Supporting Information

Stabilizing Bi active Species via Constructing Bi-O-Ce Interface for Enhanced CO_2 Electroreduction to Formate

Xinya Ren, She Gong, Zhenze Han, Yu Wei* and Yan Gao*

State Key Laboratory of Fine Chemicals, Frontier Science Center for Smart Materials, School of Chemical Engineering, Dalian University of Technology, Dalian 116024, China. E-mail: weiyu@dlut.edu.cn; dr.gaoyan@dlut.edu.cn

Experimental

Chemicals and reagents

All chemical reagents, including bismuth acetate ($C_6H_9BiO_6$, 99.9%), cerium (III) nitrate hexahydrate ($Ce(NO_3)_3 \cdot 6H_2O$, 99.5%), hexamethylenetetramine ($C_6H_{12}N_4$, 99.9%), absolute ethanol (C_2H_5OH, 99.9%), ethylene glycol ($C_2H_6O_2$, 99.9%), and potassium bicarbonate ($KHCO_3$, 99.5%), were of analytical grade and used as received without further purification.

synthesis of CeO_2@BOC

The CeO_2@BOC catalyst was synthesized via a one-step hydrothermal method. Typically, 1 mmol of bismuth acetate, 0.05 mmol of cerium nitrate hexahydrate, and 125 mg of hexamethylenetetramine (HMT) were dispersed in a mixed solvent system containing 14 mL of ethanol and 14 mL of ethylene glycol under continuous magnetic stirring at 1000 rpm until a clear solution was obtained. The resulting mixture was then transferred into a 50 mL Teflon-lined stainless steel autoclave and heated in an oven at 170 °C for 8 h. After the autoclave cooled down to room temperature naturally, the resulting precipitate was collected and washed thoroughly with ethanol and deionized water three times each via centrifugation. The final product was dried in a vacuum oven at 70 °C for 2 h, yielding a light-yellow powder denoted as CeO_2@BOC.

A series of x% CeO_2@BOC electrocatalysts (where x represents the molar ratio of Ce/(Ce+Bi)) were prepared using the identical procedure by varying only the amount of cerium nitrate precursor.

synthesis of BOC

The control sample, denoted as BOC, was prepared using an identical procedure to that of CeO2@BOC, with the only exception that no cerium source was added. The resulting product was an off-white powder.

synthesis of CeO_2

The CeO_2 control sample was prepared using an identical procedure to that of CeO_2@BOC, with the only exception that no bismuth source was added. The resulting product was a light-yellow powder.

Fabrication of the electrodes

5 mg of catalysts, and 20 μL of 5wt% Nafion solution was dispersed into 1 mL isopropyl alcohol, followed by sonication for 60 min to form a homogeneous solution. Then 100 μL of the as-prepared solution was dropped onto a carbon paper with the area of 1×1 cm2 and dried at 60°C for 0.5h to obtain the catalytic electrode.

Materials characterizations

The morphology and dimension of as-prepared materials were characterized by Nova Nano SEM 450 equipment. The microstructures of the samples were characterized by TEM (FEI TF30). X-ray diffraction (XRD) pattern was collected by a D/max-2400 diffractometer (Japan Rigaku Rotaflex) using Cu Kα radiation (λ = 154.1 nm). X-ray photoelectron spectroscopy (XPS) measurement was performed on a Thermo ESCALAB XI+ instrument. The binding energy (BE) was calibrated with respect to the C 1s level (284.8 eV) of adventitious carbon. Fourier Transform Infrared (FT-IR) spectroscopy was performed using the standard KBr pellet method to characterize the vibrational modes of the chemical bonds. Meanwhile, Electron Paramagnetic Resonance (EPR) spectroscopy was utilized to determine the presence of unpaired electrons by detecting paramagnetic signals, with the powder sample contained in a quartz tube for analysis.

Electrochemical measurements

All electrochemical measurements were run on a CHI 760E electrochemical workstation. The H-type cell was composed with two chambers separated by Nafion 117 membrane. The prepared electrode was subjected as the cathode in the catholyte chamber and a platinum wire as the counter electrode in the anolyte chamber. Saturated Ag/AgCl electrode was employed as the reference electrode, and CO_2 saturated 0.5 M $KHCO_3$ with a pH of 8.34 was used as the electrolyte. Solution resistance and charge transfer resistance were determined by electrochemical impedance spectroscopy at frequency ranges from 0.1 Hz to 100 KHz. All potentials measured against Ag/AgCl were converted to RHE scale using the formula:

$$E_{RHE} = E_{Ag/AgCl} + 0.198 + 0.0591pH \tag{16}$$

The flow cell consists of a gas chamber, a catholyte chamber, and an anolyte chamber. Each chamber has an inlet and outlet for the feed of CO_2 gas or for the circulation of electrolyte. The exposed window for electrode is 1×1 cm^2. 1 M KOH aqueous solution was used as both anolyte and catholyte and the two chambers were separated with Nafion 117 membrane. An electronic flowmeter was employed to control the flow rate of CO_2 gas. A gas diffusion layer (YLS-30T) was used, and the mass loading is around 1 mg cm^{-2}.

The calculation of electrochemical surface area (ECSA)

All ECSA measurement ranges in this paper are within the non-Faradaic range -0.1 V to -0.2 V. The ECSA was derived from the double layer capacitance (C_{dl}), where the double layer capacitance can be obtained by conducting cyclic voltammetry (CV) at various scan rates in the non-faradaic region. The calculation formula is as follows:

$$C_{dl} = \left[\Delta(j_a - j_c)\right] / 2\Delta V \tag{17}$$

Where C_{dl} represents double layer capacitance, j_a represents anodic current at a specified potential, j_c represent cathodic current at the same potential, ΔV represents the difference of scan rates[1].

Determination of gaseous products and liquid products

The gas products were analyzed with an online gas chromatography (Fuli 9720plus) equipped with a thermal conductivity detector for H_2 detection, and a flame ionization detector for CO detection. Each quantitative sampling was performed for three times to achieve accurate results. Liquid products are detected by ion chromatograph (Shenghan CIC-D100).

The Faradaic efficiency (FE) of H_2 or CO is calculated with the following formula:

$$FE = \left(\frac{Q}{Q_{total}}\right) \times 100\% = A \times R \times V_g \times t \times F \times 2/V_M \tag{18}$$

where A is the area of H_2 or CO from GC data, R is the correction factor, V_g is the flow rate of gas, t is the period of electrolysis, F is the Faraday constant of 96485 C mol^{-1}, and V_M of 24500 ml mol^{-1} represents the volume of gas per mole under test conditions. The formate FE ($FE_{Formate}$) is calculated with the following formula：

$$FE_{formate} = 2nF/Q \tag{19}$$

where 2 represents the number of transferred electrons during the reaction; n represents $ERCO_2$ to form formate; F is the Faraday constant (96500C mol-1); and Q is the total amount of reaction charge[2].

In situ Raman measurements

The measurement was carried out by utilizing a home-made spectro-electrochemical flow cell through a quartz window to detect the cathode GDL. A piece of catalysts supported on GDL (2 × 2 cm^2, loading mass: 1.0 mg cm^{-2}) was inserted through the wall of the cell to keep the plane of the working electrode perpendicular to the incident laser. The reference electrode was Ag/AgCl (saturated KCl) placed in the cathodic compartment; the counter electrode was a graphite rod placed in the anodic compartment. A syringe pump was used to pump 0.5 M $KHCO_3$ at a constant flow rate of 5 mL min^{-1} over the GDL. Investigate the influence of electrolysis time on the structural changes of the material: Record the spectra after electrolysis for 30 seconds, 1 min, 2 min, 3 min, 10 min, and 20 min at -0.9 V vs. RHE. Investigate the influence of electrolysis potential on the structural changes of the material: Collect the spectra after electrolysis for 10 minutes at various set potentials ranging from -0.7 to -1.2 V vs. RHE. Investigate the influence of the reaction intermediate on changes with electrolysis potential: Collect the spectra after electrolysis for 10 min at OCP and at various set potentials ranging from -0.6 to -1.2 V vs. RHE.

Supplementary Figures

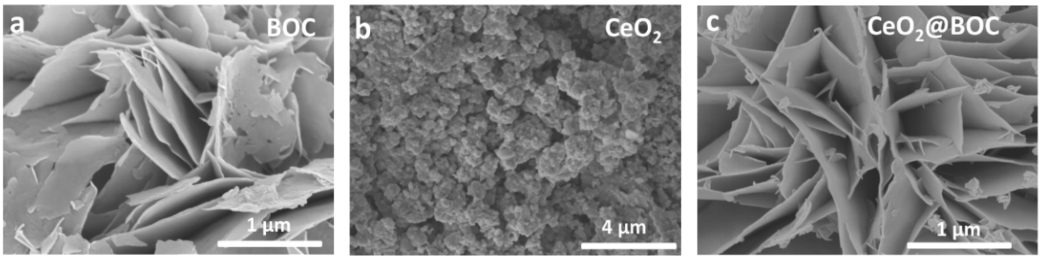

Figure S1. SEM image of (a) BOC, (b) CeO_2 and (c) CeO_2@BOC.

As shown in the figures, BOC exhibits well-defined and smooth nanosheet structures (Fig. S1a), while CeO_2 presents irregular nanoparticle morphologies (Fig. S1b).

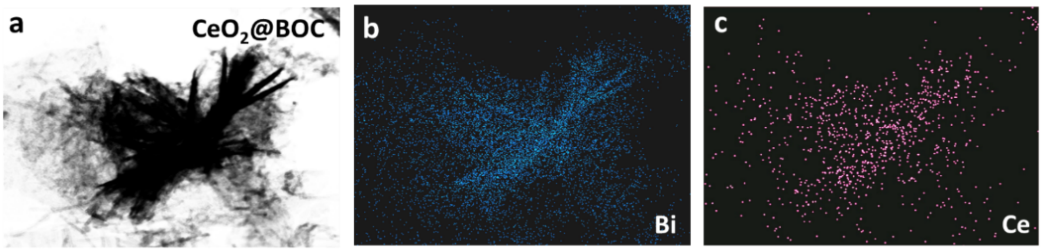

Figure S2. (a-c) EDS elemental mapping of CeO_2@BOC.

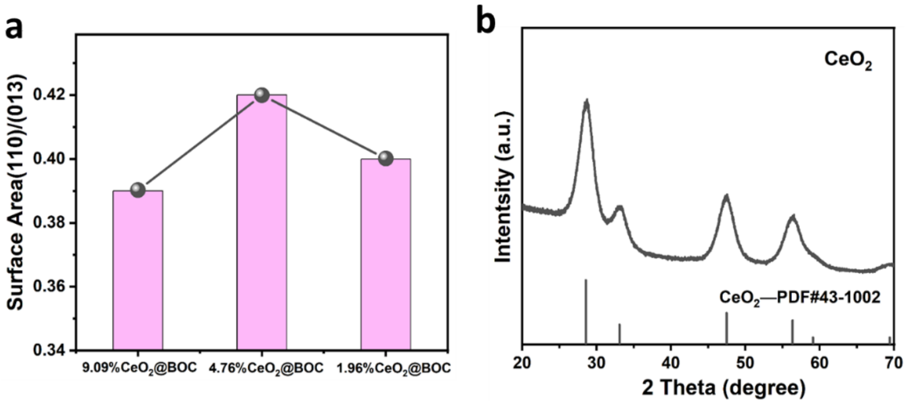

Figure S3. (a) Area ratio of (110) crystal plane and (013) crystal plane of the catalysts prepared under different reaction conditions; (b) XRD pattern of CeO_2.

No distinct CeO_2 diffraction peaks are observed in CeO_2@BOC, likely due to the low content and the similar lattice parameters of CeO_2 and BOC. As shown in Fig. S3b, the XRD pattern of pure CeO_2 displays characteristic peaks at 28.554°, 33.081°, and 47.478°, corresponding to the (111), (200), and (220) planes of CeO_2, respectively[3].

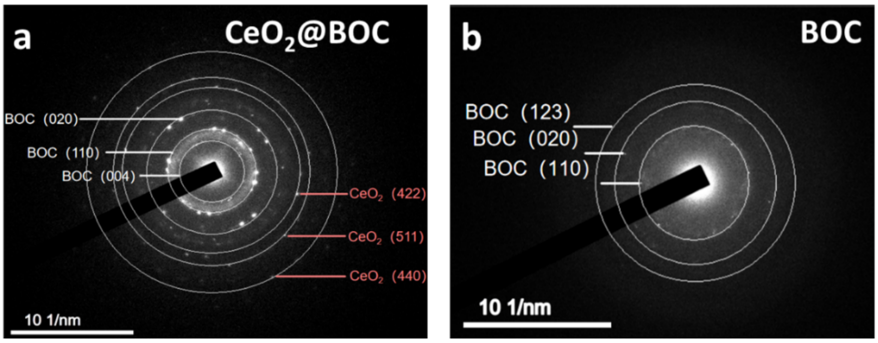

Figure S4. (a) SAED pattern of CeO_2@BOC and (b) BOC

The SAED patterns of CeO_2@BOC and BOC show symmetrical diffraction spots assigned to the (110) and (020) planes of BOC. In the SAED pattern of CeO_2@BOC, additional spots corresponding to the CeO_2 (422) and (511) planes are also detected.

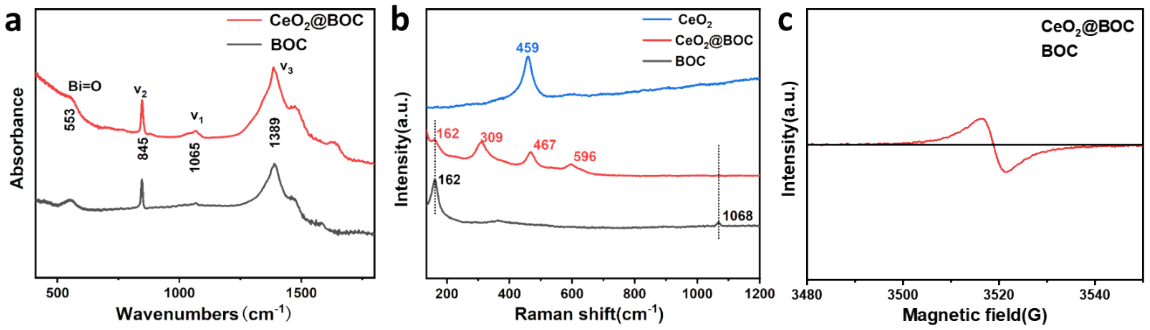

Figure S5. (a) FTIR spectra of CeO_2@BOC and BOC; (b) Raman spectra of CeO_2@BOC, BOC, and CeO_2; (c) EPR spectra of CeO_2@BOC and BOC.

The FTIR spectra of BOC and CeO_2@BOC (Fig. S5a) exhibit an absorption peak at 1389 cm^{-1} corresponding to the antisymmetric vibration (ν_3) of CO_3^{2-}, while the peak at 845 cm^{-1} is assigned to the out-of-plane bending vibration (ν_2) of CO_3^{2-}. The peak at 1065 cm^{-1} originates from the symmetric stretching vibration (ν_1) of CO_3^{2-}, and the band at 553 cm^{-1} is attributed to the stretching vibration of the Bi=O bond. The Raman spectra (Fig. S5b) show two characteristic peaks at 162 and 1068 cm^{-1}, confirming the formation of BOC, and he strong peak at 1068 cm^{-1} is assigned to the ν_1 vibration of chemisorbed carbonates[4]. In the Raman spectrum of CeO2@BOC, the peak at 467 cm^{-1} is attributed to the F_{2g} vibrational mode of fluorite-structured CeO_2[5]. The feature at 596 cm^{-1} corresponds to defect-induced oxygen vacancies[6]. Furthermore, EPR analysis (Fig. S5c) provides additional evidence for the presence of oxygen vacancies in CeO_2@BOC.

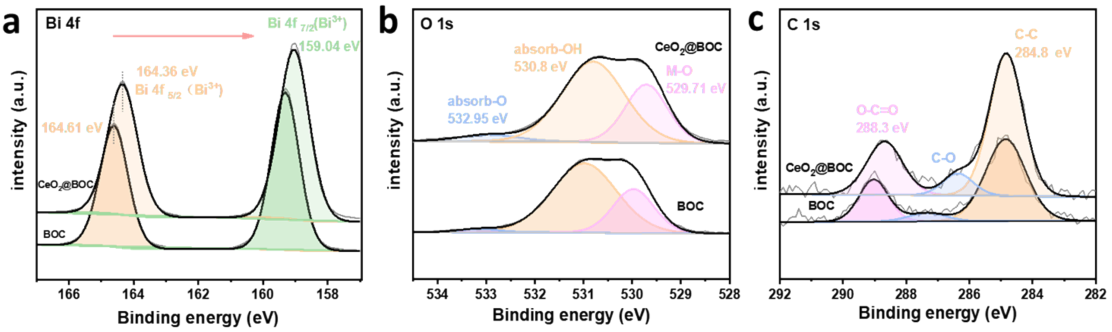

Figure S6. XPS spectrum of CeO_2@BOC and BOC: (a) Bi 4f, (b) O 1s and (c) C 1s.

The signals of Bi, O, Ce, and C are all detected in the synthesized samples. In the Bi 4f spectrum, the characteristic peaks at 159.04 eV and 164.35 eV correspond to the Bi $4f_{7/2}$ and Bi $4f_{5/2}$ orbitals of Bi^{3+}The O 1s spectra exhibit peaks corresponding to lattice oxygen and surface-adsorbed oxygen species[7]. In the C 1s spectra, the peaks at binding energies of 284.8 eV, 286.3 eV, and 288.3 eV can be assigned to C-C, C-O, and O-C=O species, respectively[8]. The peaks at 288.3 eV and 284.8 eV correspond to carbonates and amorphous carbon, respectively[9].

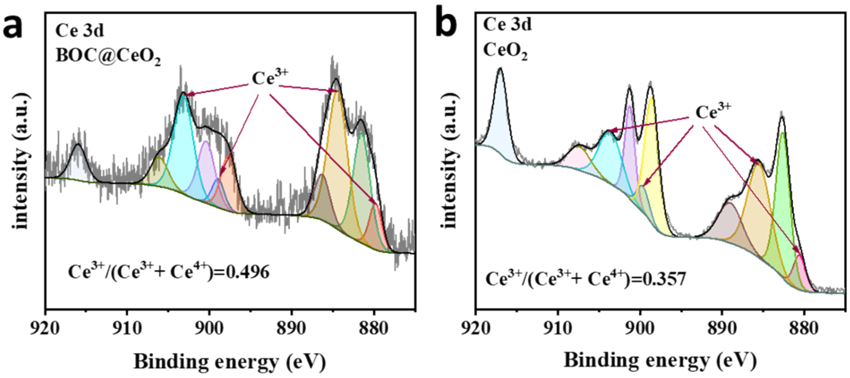

Figure S7. XPS spectra of BOC(a) and CeO_2@BOC(b): Ce 3d.

The Ce 3d spectrum[10] contains two sets of spin–orbit doublets corresponding to Ce $3d_{3/2}$ (u) and Ce $3d_{5/2}$ (v). The u’ and v’ peaks are characteristic of Ce^{3+}, while the peaks u, u”, u‴, v, v”, and v‴ are associated with Ce^{4+}. Based on this, the peaks for Ce^{3+} have been labeled in the figure, enabling integration calculations to determine $Ce^{3+}/(Ce^{3+}+Ce^{4+})$ proportion.

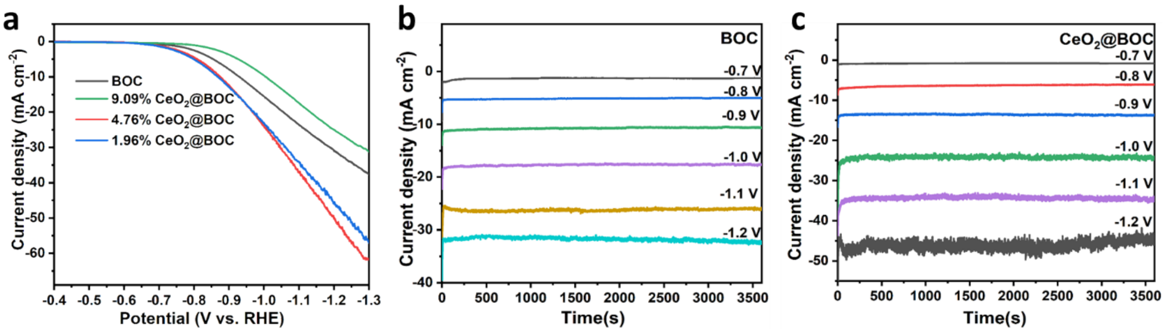

Figure S8. (a) Linear sweep voltammograms of catalysts with different cerium-bismuth ratios under saturated carbon dioxide conditions; Current-time curves of (b) BOC and (c) CeO_2@BOC at different voltages.

To further assess the product selectivity, 1 h chronoamperometry tests were carried out in CO_2-saturated electrolyte at potentials ranging from -0.7 to -1.2 V vs. RHE. The I-T curves (Figure S4b-c) show that both BOC and CeO_2@BOC maintain stable electrolysis throughout the test.

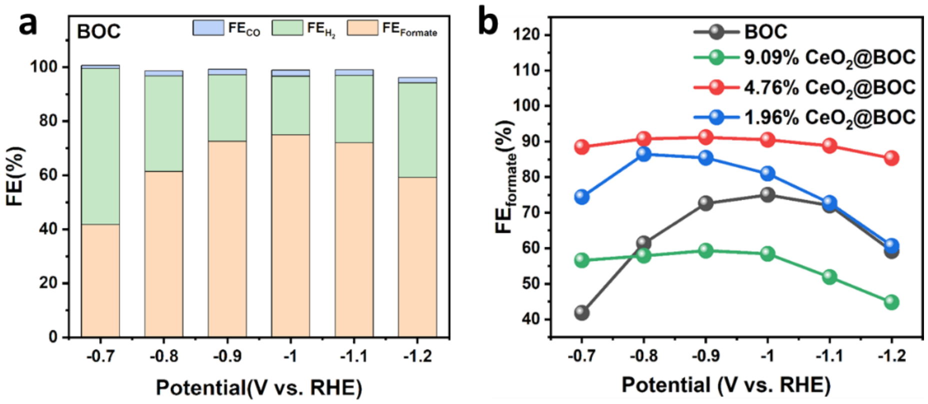

Figure S9. (a) Faradaic efficiencies of various products for BOC; (b) Methanation Faraday efficiencies of catalysts with different cerium-bismuth ratios at different voltages

The formate Faradaic efficiency of BOC but remains below 75% across the entire potential range.

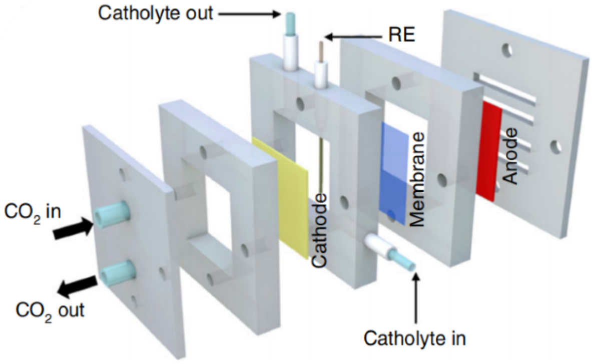

Figure S10. The schematic illustration of the flow-cell configuration

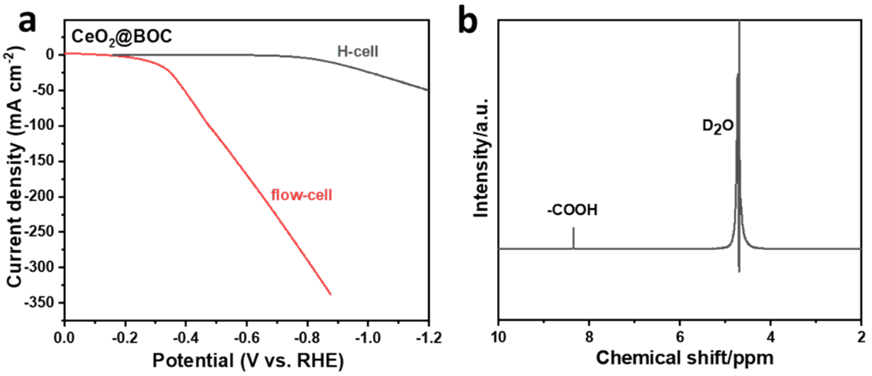

Figure S11. (a) LSV curves of CeO_2@BOC in an H-cell and a flow cell; (b) NMR spectra of the liquid products at high current density

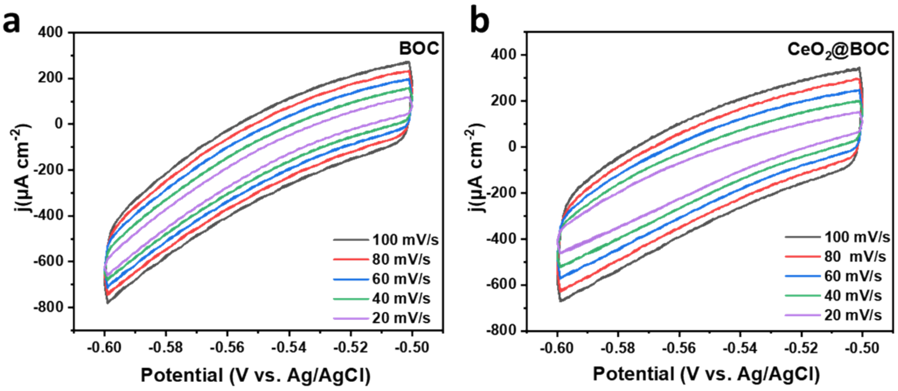

Figure S12. Cyclic voltammograms of BOC(a) and CeO_2@BOC(b) in the non-Faradaic potential region, at scan rates of 20, 40, 60, 80, and 100 mV s^{-1}.

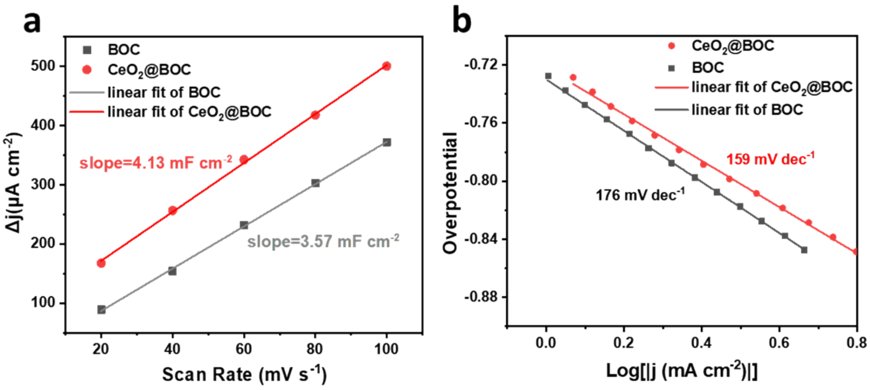

Figure S13. (a) C_{dl} fitting for BOC and CeO_2@BOC; (b) Tafel plots of CeO_2@BOC and BOC.

The Tafel plots (Fig. S13b) show that the Tafel slopes of all samples exceed 118 mV dec^{-1}, indicating that they share the same rate-determining step, namely the formation of the $*CO_2^-$ intermediate[11].

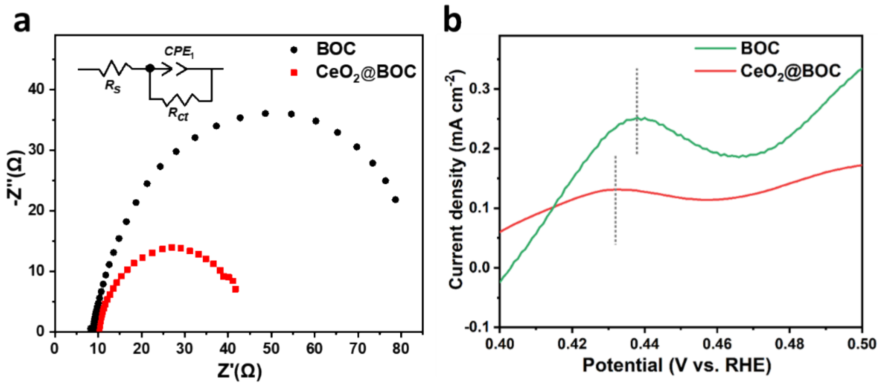

Figure S14. (a) EIS spectra of CeO_2@BOC and BOC; (b) OH^- adsorption measurements of

CeO_2@BOC and BOC in Ar-saturated electrolyte. Therefore, single-oxidation LSV was performed in Ar-saturated 0.1 M NaOH to assess the OH- adsorption behavior

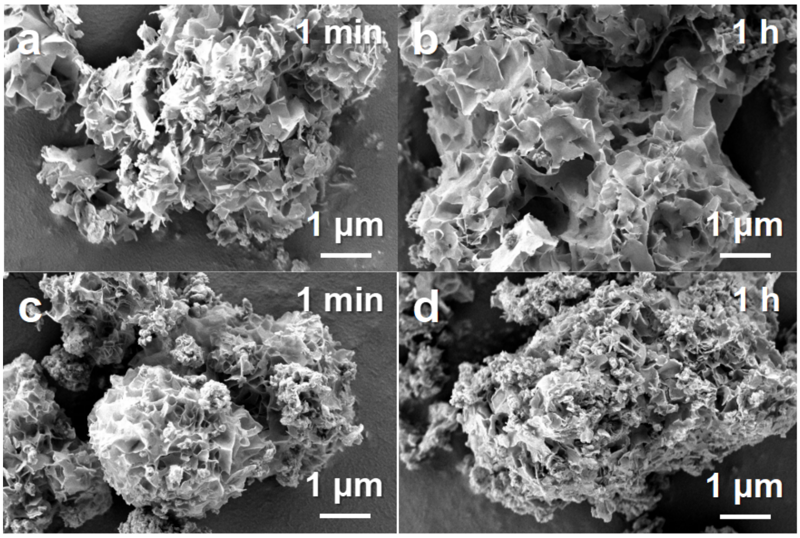

Figure S15. SEM images of CeO_2@BOC after electrolysis for (a) 1 min and (b) 1 h, and of BOC after electrolysis for (c) 1 min and (d) 1 h.

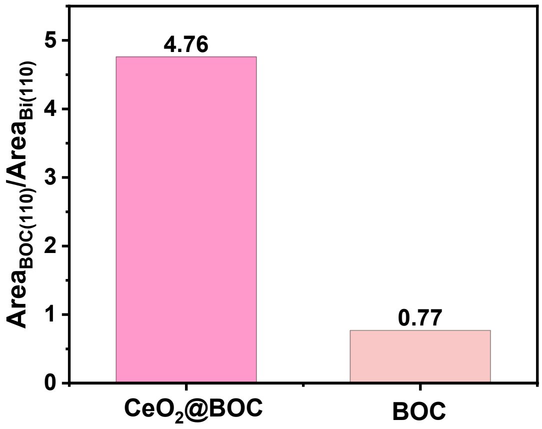

Figure S16. Relative proportions of the Bi (110) metallic phase and the BOC (110) facet in CeO_2@BOC after the reaction.

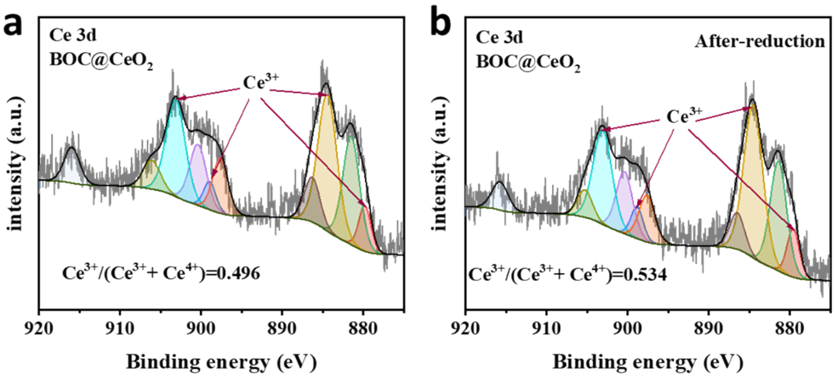

Figure S17. (a) XPS Ce 3d spectrum of CeO$_2$@BOC before the reaction; (b) XPS Ce 3d spectrum of CeO$_2$@BOC after the reaction.

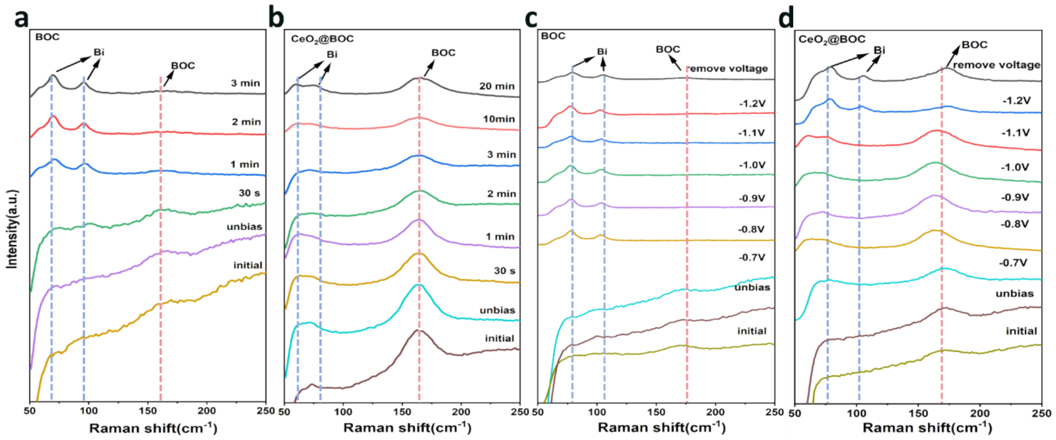

Figure S18. (a-b) operando Raman spectra of CeO$_2$@BOC and BOC at different electrolysis durations and (b-c) operando Raman spectra of CeO$_2$@BOC and BOC under different applied potentials.

Table S1. Performance and stability of similar catalysts reported in recent years.

Catalysts	FE% (Formate)	j (mA cm^{-2})	Stability (h)	Cell Type	Ref.
CeO$_2$@BOC	>90%	225	120	Flow-Cell	This work
BiNS	95%	24	10	H-cell	[12]
Bi$_2$O$_3$/BiO$_2$	95.4	220	30	H-cell	[13]
Bi MP	95	271.7	10	Flow-cell	[14]
In/Bi-750	90.82	200	13	Flow-cell	[15]
BiOBr	96	90	1.94	Flow-cell	[16]
BOC NFs	97	230	5	MEA	[17]
BBS	95	400	2.78	Flow-cell	[18]
Bi-ene	99.8	100	3	Flow-cell	[19]
Bi$_2$O$_3$@C-800	93	200	10	Flow-cell	[20]
Bi$_{0.1}$Sn	95	100	2400	Flow-cell	[21]

2D-Bi	99	17.3	10	H-cell	22
BOC-NSs	93	930	12	H-cell	23
CuO/F/C(w)	56.8	145	10	H-cell	24
$Bi_{0.6}Cu_{0.4}$ NSs	99.23	260	400	H-cell	25
Cu_2-C-1100-4	63.4	180	14	MEA	26

We compared the performance and stability of our catalyst with similar catalysts reported in recent years. The results demonstrate that our catalyst simultaneously achieves >90% high Faradaic efficiency, a high catalytic current density of 225 mA cm^{-2}, and exceptional long-term stability of 120 hours. The comprehensive performance of these three indicators ranks among the top of all catalysts in the table.

References

1. W. Zhang, Y. Hu, L. Ma, G. Zhu, P. Zhao, X. Xue, R. Chen, S. Yang, J. Ma, J. Liu and Z. Jin, *Nano Energy*, 2018, **53**, 808-816.
2. P. Su, W. Xu, Y. Qiu, T. Zhang, X. Li and H. Zhang, *ChemSusChem*, 2018, **11**, 848-853.
3. J. L. DiMeglio and J. Rosenthal, *J. Am. Chem. Soc.*, 2013, **135**, 8798-8801.
4. I. V. Chernyshova, P. Somasundaran and S. Ponnurangam, *Proc. Natl. Acad. Sci. U.S.A.*, 2018, **115**, 9261-9270.
5. S. Wu, M. Tian, Y. Hu, N. Zhang, W. Shen, J. Li, L. Guo, P. Da, P. Xi and C.-H. Yan, *Inorg. Chem.*, 2023, **62**, 4088-4096.
6. H. Sun, H. Wang and Z. Qu, *ACS Catal.*, 2023, **13**, 1077-1088.
7. S. Liu, Y. Fan, Y. Wang, S. Jin, M. Hou, W. Zeng, K. Li, T. Jiang, L. Qin, Z. Yan, Z. Tao, X. Zheng, C. Shen, Z. Liu, T. Ahmad, K. Zhang and W. Chen, *Nano Lett.*, 2022, **22**, 9107-9114.
8. L. Li, C. Lai, F. Huang, M. Cheng, G. Zeng, D. Huang, B. Li, S. Liu, M. Zhang, L. Qin, M. Li, J. He, Y. Zhang and L. Chen, *Water Res.*, 2019, **160**, 238-248.
9. Y. Lan, Z. Li, W. Xie, D. Li, G. Yan, S. Guo, C. Pan and J. Wu, *J. Hazard. Mater.*, 2020, **385**, 121622.
10. M. Konsolakis, *Appl. Catal. B Environ. Energy.*, 2016, **198**, 49-66.
11. J. Xue, X. Fu, S. Geng, K. Wang, Z. Li and M. Li, *J. Environ. Manag.*, 2023, **342**, 118354.
12. N. Han, Y. Wang, H. Yang, J. Deng, J. Wu, Y. Li and Y. Li, *Nat. Commun.*, 2018, **9**, 1320.
13. X. Feng, H. Zou, R. Zheng, W. Wei, R. Wang, W. Zou, G. Lim, J. Hong, L. Duan and H. Chen, *Nano Lett.*, 2022, **22**, 1656-1664.
14. C. Lin, Y. Liu, X. Kong, Z. Geng and J. Zeng, *Nano Res.*, 2022, **15**, 10078-10083.
15. Q. Wang, X. Yang, H. Zang, C. Liu, J. Wang, N. Yu, L. Kuai, Q. Qin and B. Geng, *Small*, 2023, **19**, 2303172.
16. S. Yang, H. An, S. Arnouts, H. Wang, X. Yu, J. de Ruiter, S. Bals, T. Altantzis, B. M. Weckhuysen and W. van der Stam, *Nat. Catal.*, 2023, **6**, 796-806.
17. P. F. Sui, M. R. Gao, S. Liu, C. Xu, M. N. Zhu and J. L. Luo, *Adv. Funct. Mater.*, 2022, **32**, 2203794.

18. L. Lv, R. Lu, J. Zhu, R. Yu, W. Zhang, E. Cui, X. Chen, Y. Dai, L. Cui, J. Li, L. Zhou, W. Chen, Z. Wang and L. Mai, *Angew. Chem. Int. Ed.*, 2023, **62**, e202303117.
19. C. Cao, D. D. Ma, J. F. Gu, X. Xie, G. Zeng, X. Li, S. G. Han, Q. L. Zhu, X. T. Wu and Q. Xu, *Angew. Chem. Int. Ed.*, 2020, **59**, 15014-15020.
20. P. Deng, F. Yang, Z. Wang, S. Chen, Y. Zhou, S. Zaman and B. Y. Xia, *Angew. Chem. Int. Ed.*, 2020, **59**, 10807-10813.
21. L. Li, A. Ozden, S. Guo, F. P. García de Arquer, C. Wang, M. Zhang, J. Zhang, H. Jiang, W. Wang, H. Dong, D. Sinton, E. H. Sargent and M. Zhong, *Nat. Commun.*, 2021, **12**, 5223.
22. C. Xia, P. Zhu, Q. Jiang, Y. Pan, W. Liang, E. Stavitski, H. N. Alshareef and H. Wang, *Nat. Energy*, 2019, **4**, 776-785.
23. T. Fan, W. Ma, M. Xie, H. Liu, J. Zhang, S. Yang, P. Huang, Y. Dong, Z. Chen and X. Yi, *Cell Rep. Phys. Sci.*, 2021, **2**, 100353.
24. X. Huang, X. Li, S. Yan, D. Wang, C. Long, Y. Ying, P. An, Z. Guo, Q. Li, C. Yang, S. Chen, J. Han, L. Chang, S. Lu and Z. Tang, *Sci. Adv.*, 2025, **11**, eads0609.
25. H. Liu, Y. Bai, M. Wu, Y. Yang, Y. Wang, L. Li, J. Hao, W. Yan and W. Shi, *Angew. Chem. Int. Ed.*, 2024, **63**, e202411575.
26. Y. Li, Z. Pei, D. Luan and X. W. Lou, *Angew. Chem. Int. Ed.*, 2023, **62**, e202302128.